

Space-geodetic evidence for multiple magma reservoirs and subvolcanic lateral intrusions at Fernandina Volcano, Galápagos Islands

Marco Bagnardi¹ and Falk Amelung¹

Received 23 May 2012; revised 12 September 2012; accepted 13 September 2012; published 27 October 2012.

[1] Using Interferometric Synthetic Aperture Radar (InSAR) measurements of the surface deformation at Fernandina Volcano, Galápagos (Ecuador), acquired between January 2003 and September 2010, we study the structure and the dynamics of the shallow magmatic system of the volcano. Through the analysis of spatial and temporal variations of the measured line-of-sight displacement we identify multiple sources of deformation beneath the summit and the southern flank. At least two sources are considered to represent permanent zones of magma storage given their persistent or recurrent activity. Elastic deformation models indicate the presence of a flat-topped magma reservoir at ~ 1.1 km below sea level and an oblate-spheroid cavity at ~ 4.9 km b.s.l. The two reservoirs are hydraulically connected. This inferred structure of the shallow storage system is in agreement with previous geodetic studies and previous petrological analysis of both subaerial and submarine lavas. The almost eight-year-long observation interval provides for the first time geodetic evidence for two subvolcanic lateral intrusions from the central storage system (in December 2006 and August 2007). Subvolcanic lateral intrusions could provide the explanation for enigmatic volcanic events at Fernandina such as the rapid uplift at Punta Espinoza in 1927 and the 1968 caldera collapse without significant eruption.

Citation: Bagnardi, M., and F. Amelung (2012), Space-geodetic evidence for multiple magma reservoirs and subvolcanic lateral intrusions at Fernandina Volcano, Galápagos Islands, *J. Geophys. Res.*, 117, B10406, doi:10.1029/2012JB009465.

1. Introduction

[2] Six volcanoes in the western Galápagos Islands of Isabela and Fernandina have shown clear signs of active deformation since their geodetic monitoring began [Amelung *et al.*, 2000; Geist *et al.*, 2006a] and three of them have erupted since 2005. Among these, Fernandina can be considered the most active volcano in the archipelago, having experienced 25 eruptions in the past two centuries and three eruptions since 1995 [Jónsson *et al.*, 1999; Rowland *et al.*, 2003; Chadwick *et al.*, 2011; Smithsonian Institution, Bulletin of the Global Volcanism Network, monthly reports for Fernandina volcano, 1995–2012, available at <http://www.volcano.si.edu>]. However, the eruptive activity involves only a fraction of the magma coming from the mantle. Large portions of the fluid are in fact stored in crustal reservoirs or intruded laterally within the volcanic edifice, and knowing where and how the un-erupted magma is stored or intruded become fundamental aspects in the study of the volcanic

activity. For example, Fernandina is the site of one of the largest caldera collapses on a basaltic volcano in recorded history (June 1968, ~ 350 m over a 12-day period), but the cause of this event remains enigmatic [Simkin and Howard, 1970; Filson *et al.*, 1973; Rowland and Munro, 1992; Howard, 2010]. For a caldera collapse to occur magma has to be removed from a reservoir, usually through a volcanic eruption. Although the 1968 collapse at Fernandina was preceded by two eruptions, the volume of lava and ash erupted during these events was more than 100 times smaller than the estimated volume of the collapse. Therefore, another process for magma withdrawal in addition to the eruptions must be taken into account to explain the volume of the collapse.

[3] The presence of a large caldera is the evidence that each of the seven volcanoes of the western Galápagos Islands has a shallow magma reservoir beneath the summit, however, the remaining portion of their storage system is not fully understood. From integrative geophysical and petrologic studies the Galápagos volcanoes can be divided based on their evolutionary stage [Geist, 2011]. Fernandina, together with Sierra Negra and Wolf, is considered a mature, monotonic volcano erupting strongly evolved tholeiites. Through time, magma evolution and crystallization would create a growing mush pile several kilometers thick and magmas would transit through this pile before residing in the shallow subcaldera reservoir [Geist *et al.*, 2006b]. Petrologic models also suggest the presence of deeper zones of crustal

¹Division of Marine Geology and Geophysics, Rosenstiel School of Marine and Atmospheric Science, University of Miami, Miami, Florida, USA.

Corresponding author: M. Bagnardi, Division of Marine Geology and Geophysics, Rosenstiel School of Marine and Atmospheric Science, University of Miami, 4600 Rickenbacker Cswy., Miami, FL 33149, USA. (mbagnardi@rsmas.miami.edu)

©2012. American Geophysical Union. All Rights Reserved.
0148-0227/12/2012JB009465

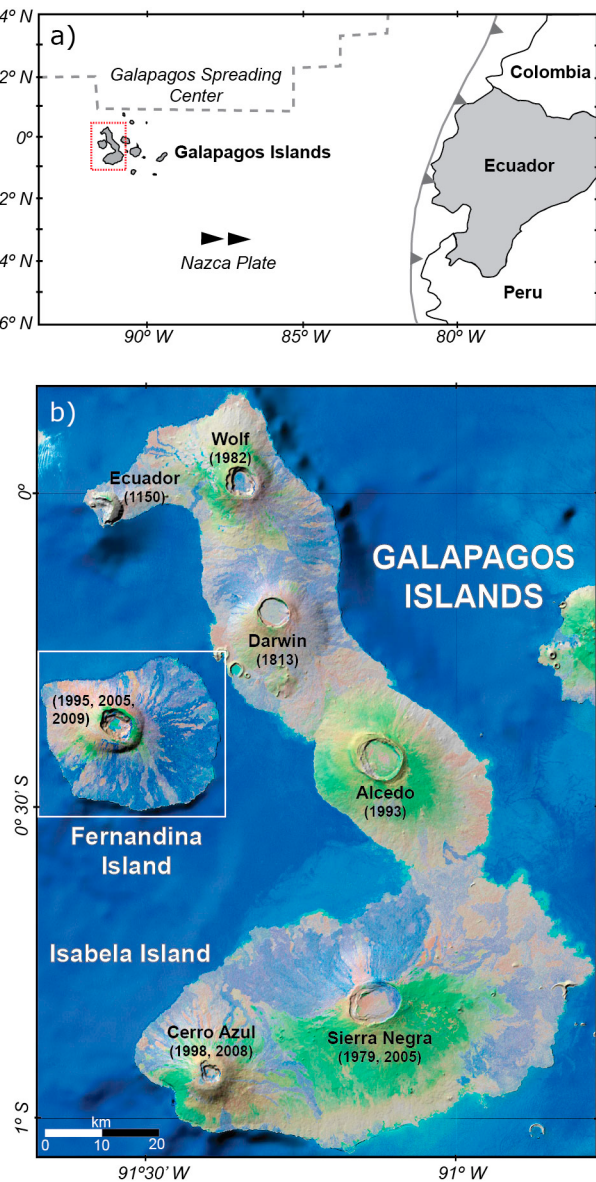


Figure 1. (a) Map showing the location of the Galápagos Islands relatively to South America and the Galápagos Spreading Center (GSC). Black arrows indicate the motion of the Nazca Plate (91°) relative to the global hot spot reference frame. (b) Map of the western islands of the Galápagos Archipelago (Landsat 7 shaded-relief color composite image; bathymetry: GEBCO_08 Grid, version 20100927, <http://www.gebco.net>; topography: hole-filled seamless SRTM data V4). Six volcanoes on Isabela and Fernandina islands have been actively deforming during the last decade, and three of them erupted. For each volcano, dates of the latest eruptions are reported. The white square marks the area covered by subsequent figures in this paper.

storage where magma undergoes cooling and fractionation [Geist *et al.*, 1998] and evidence for at least a second, discrete magma reservoir is provided by geodetic measurements [Chadwick *et al.*, 2011]. A multiple magma reservoir system would make Fernandina different from Sierra Negra where only one subcaldera reservoir is inferred from the measured

deformation [Amelung *et al.*, 2000; Yun *et al.*, 2006; Jónsson, 2009] and no evidence for deeper sources has been found.

[4] In this paper, the different aspects of the volcanic activity at Fernandina are studied by looking at their surface expression as ground deformation. Favorable ground conditions (scarce vegetation, surface mostly covered by lava) provide a good opportunity for the use of detailed Interferometric Synthetic Aperture Radar (InSAR) measurements when studying the surface deformation. We use Synthetic Aperture Radar (SAR) data acquired by the European Space Agency's ENVISAT satellite between January 2003 and September 2010, a longer time-interval than any previous geodetic studies at Fernandina. This period spans two eruptions and 18 major earthquakes (M_w 3.8–5.4), with epicenters located within 100 km from the summit of the volcano. Most of this seismicity is clustered in two seismic swarms that accompany broad and rapid deformation of the volcanic edifice. Temporal and spatial variations in the surface displacement are studied using InSAR time series and through the analysis of single interferograms. Data acquired from different viewing geometries and frequent repeat passes of the satellite provide the opportunity to observe the same events from different perspectives and better study the timing of each event.

[5] Our findings suggest that the un-erupted magma is stored in multiple crustal reservoirs, hydraulically connected and centered at different depths below the summit caldera. Surface deformation recorded during periods of inflation or deflation is used to study variations in the excess magma pressure within the magma plumbing system. We also identify the occurrence of subvolcanic lateral intrusions accompanied by seismic swarms, and provide for the first time geodetic evidence for this type of activity in the Galápagos. These intrusions cause the withdrawal of large quantities of magma from the storage system and may play an important role for the development of the Galápagos volcanic system.

2. Geologic Setting

[6] The Galápagos Archipelago is a cluster of 13 major (>100 ha) basaltic volcanic islands located near the equator on the eastward-moving Nazca plate, 1000 km west of Ecuador (Figure 1a). These islands sit on a shallow submarine platform that rises for more than 2000 m above the surrounding ocean floor. It is believed that the volcanoes have grown above a hot spot now placed on the southern side of the E-W trending Galápagos Spreading Center (GSC), and centered under Fernandina and Isabela Islands [Wilson, 1963; Morgan, 1971; Hey, 1977; Villagómez *et al.*, 2007]. Fernandina and the other western Galápagos volcanoes (Figure 1b) represent the type locality for the “Galápagos shield volcano”: edifices are characterized by steep upper flanks, proportionately large calderas, arcuate summit fissures, and radial flank fissures [Simkin, 1984; Chadwick and Howard, 1991].

[7] Fernandina Island, with a diameter of about 30 km and maximum elevation of 1476 m, is the westernmost eruptive center in the archipelago, and has a very well developed subaerial circumferential and radial fissure system (blue lines in Figure 2a), probably the most evident of all the

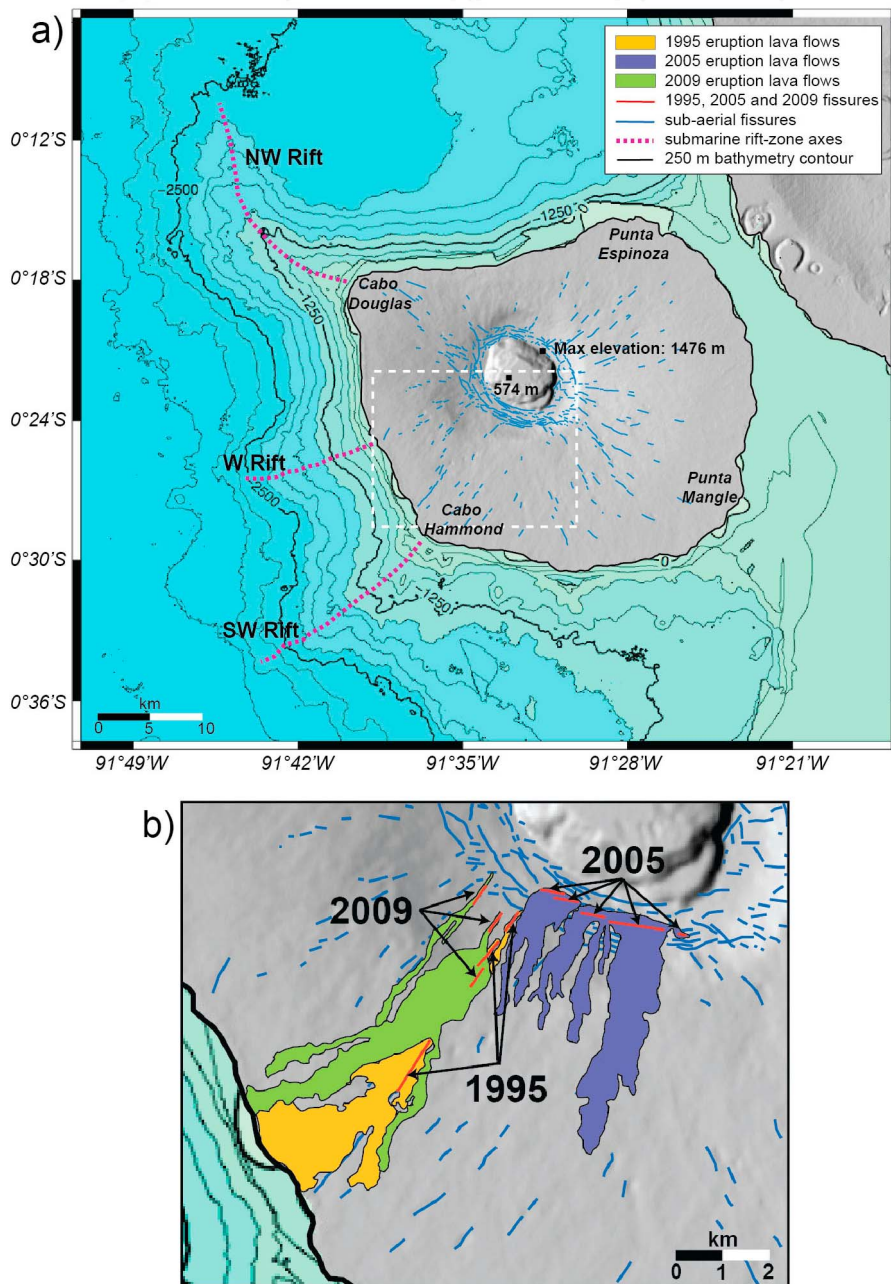


Figure 2. (a) Shaded relief map of Fernandina Island and bathymetry (topography: hole-filled seamless SRTM data V4; bathymetry: multibeam data from NGDC-NOAA, <http://map.ngdc.noaa.gov/>). Blue lines represent mapped eruptive fissures from *Chadwick and Howard* [1991]; Red-dashed lines mark submarine rift zones identified by *Geist et al.* [2006b]. (b) Blow-up of the area represented in Figure 2a with a dashed-white square and covering the location of the last three eruptions. Red solid lines mark the eruptive fissures associated with the 1995, 2005 and 2009 eruptions. The image also shows the extension of lava flows produced by these latest eruptions (yellow = 1995; purple = 2005 and green = 2009) from *Bourquin et al.* [2009] and *Chadwick et al.* [2011].

Galápagos volcanoes [*Chadwick and Howard*, 1991]. While the subaerial portion of the volcano lacks well-defined rift zones, the submarine part of Fernandina shows three well-developed rifting zones [*Geist et al.*, 2006b] that extend from the western side of the island (red dashed lines in Figure 2a).

[8] The recent eruptive activity at Fernandina includes: an eruption in 1982 from a circumferential fissure at the southern caldera rim; intracaldera eruptions in 1984, 1988 and 1991 [*Rowland and Munro*, 1992; Smithsonian Institution, Bulletin of the Global Volcanism Network, monthly reports for Fernandina volcano, 1982–2012, available at

Table 1. ENVISAT SAR Images Used in This Study to Generate Interferograms

Track (Beam, Inc. Angle)	Pass	Start Date–End Date	Acquisitions
Full Spatial Coverage			
412 (IS2, 19.2°–26.7°)	Descending	11 Feb. 2003–7 Sept. 2010	64
61 (IS2, 19.2°–26.7°)	Ascending	29 March 2003–18 Sept. 2010	68
54 (IS7, 42.5°–45.2°)	Descending	10 June 2005–11 Dec. 2009	37
147 (IS6, 39.1°–42.8°)	Ascending	20 October 2006–20 Aug. 2010	42
Partial Spatial Coverage			
104 (IS4, 31.0°–36.3°)	Ascending	14 Jun. 2005–19 May 2009	34
140 (IS2, 19.2°–26.7°)	Descending	23 Jan. 2003–10 Jun. 2010	51
376 (IS5, 35.8°–39.4°)	Ascending	3 Jul. 2005–3 May 2009	34
Total			330

<http://www.volcano.si.edu>]; an eruption on the southwestern flank from a radial fissure in 1995 [Jónsson *et al.*, 1999]; an eruption from circumferential fissures at the southern caldera rim in May 2005 [Chadwick *et al.*, 2011] and a new eruption from radial fissures in April 2009 [Bourquin *et al.*, 2009]. The trace of the eruptive fissures and the extension of the lava flows produced during the latest three eruptions are presented in Figure 2b.

[9] The elliptical summit caldera, $\sim 21 \text{ km}^2$ in area, with the $\sim 6.2 \text{ km}$ long major axis elongated in NW–SE direction and the $\sim 4.3 \text{ km}$ long minor axis directed NE–SW, is today $\sim 900 \text{ m}$ deep at its maximum, with walls sloping inward at $30\text{--}50^\circ$. The present morphology is the result of repeated cycles of partial filling and collapse, and of the down drop of the southeastern portion by as much as 350 m during the June 1968 event. A flank eruption on 21 May 1968, minor earthquake activity (m_b 3.9–4.6) through the first week of June and a large hydromagmatic explosion from the caldera wall occurred prior to this collapse, which started on 12 June. However, the estimated combined volume of the two eruptions is less than 0.2 km^3 while the volume of the collapse is equivalent to $1\text{--}2 \text{ km}^3$. No evidence of submarine eruptions during this event has been found and Simkin and Howard [1970] concluded that magma was probably withdrawn from the reservoir through lateral intrusions that didn't reach the surface.

[10] No geodetic evidence of large flank intrusions at Fernandina has ever been provided but their occurrence is suggested by the rapid uplift observed at Punta Espinoza in 1927. Here, a fishing boat anchored for the night was stranded by an uplift of “several feet” occurred in a few hours [Cullen *et al.*, 1987]. A similar event was recorded in May 1954 at the nearby Urvina Bay where the coastline of Darwin Volcano was uplifted by as much as 4.6 m and moved inland for more than a kilometer [Couffer, 1956; Richards, 1957]. The uplift occurred in less than an hour and so rapidly that fish were stranded in pools.

3. SAR Data and Processing Methods

[11] It is well recognized that InSAR is a successful geodetic technique used to measure surface deformation associated with different sources, such as earthquakes, volcanoes or anthropogenic activity [Massonnet *et al.*, 1994; Amelung *et al.*, 2000]. The phase difference (interferogram) of SAR image pairs for the same area, acquired at different times, provides measurements of the surface displacement along the radar line-of-sight (LOS) with centimeter to millimeter accuracy.

[12] We processed 330 SAR images acquired by the European Space Agency's ENVISAT satellite from four ascending and three descending tracks (Table 1), with a 35-day repeat pass. Compared to other satellites that acquired SAR images for the same area, ENVISAT provides full spatial coverage of Fernandina Island from four different viewing geometries, partial coverage from other three and the largest number of acquisitions. The sensor is a C-band SAR with an operating wavelength of 56.3 mm . Data from the three IS2 tracks are part of the ENVISAT's background mission and span the entire studied period (2003–2010). In 2005 we tasked the acquisition of data from another five tracks covering Fernandina and the neighboring Isabela Island.

[13] We use Gamma SAR Processor and Interferometry to focus the raw radar images and the JPL/Caltech ROI_PAC SAR software [Rosen *et al.*, 2004] to form interferograms. We use precise DORIS orbits provided by ESA and remove the topographic contribution to the interferometric phase using a 90 m resolution digital elevation model (DEM), re-sampled to 30 m , generated by the NASA Shuttle Radar Topography Mission (SRTM). The interferograms are phase-unwrapped using the *Snaphu* unwrapper [Chen and Zebker, 2001].

3.1. InSAR Pairs Selection and Time Series Generation

[14] To resolve the temporal evolution of surface deformation we use the small baseline subset (SBAS) method [Berardino *et al.*, 2002; Lanari *et al.*, 2004] and apply it to InSAR data from the descending (T412) and the ascending (T61) IS2 tracks, which entirely cover Fernandina Island and provide the longest temporal coverage. This method is based on the inversion of a large number of phase-unwrapped interferograms (e.g., 213 for the descending pass) to retrieve the LOS displacement history for each pixel at the epoch of each SAR acquisition.

[15] The selection of the most suitable interferometric pairs for the InSAR time series generation is performed following a multistep approach based on the key assumption of the SBAS method, for which small spatial and temporal separation between SAR acquisitions minimize decorrelation and maximize the temporal coherence of pixels [Pepe and Lanari, 2006]. For each pass we first execute a Delaunay triangulation for all possible pairs in the temporal/perpendicular baseline plane to create an interconnected network of interferograms. We remove from this selection all pairs with a perpendicular baseline larger than 400 m and successively add all possible interferograms spanning less than 300 days and with perpendicular baseline smaller than 300 m . Once all the selected interferograms are

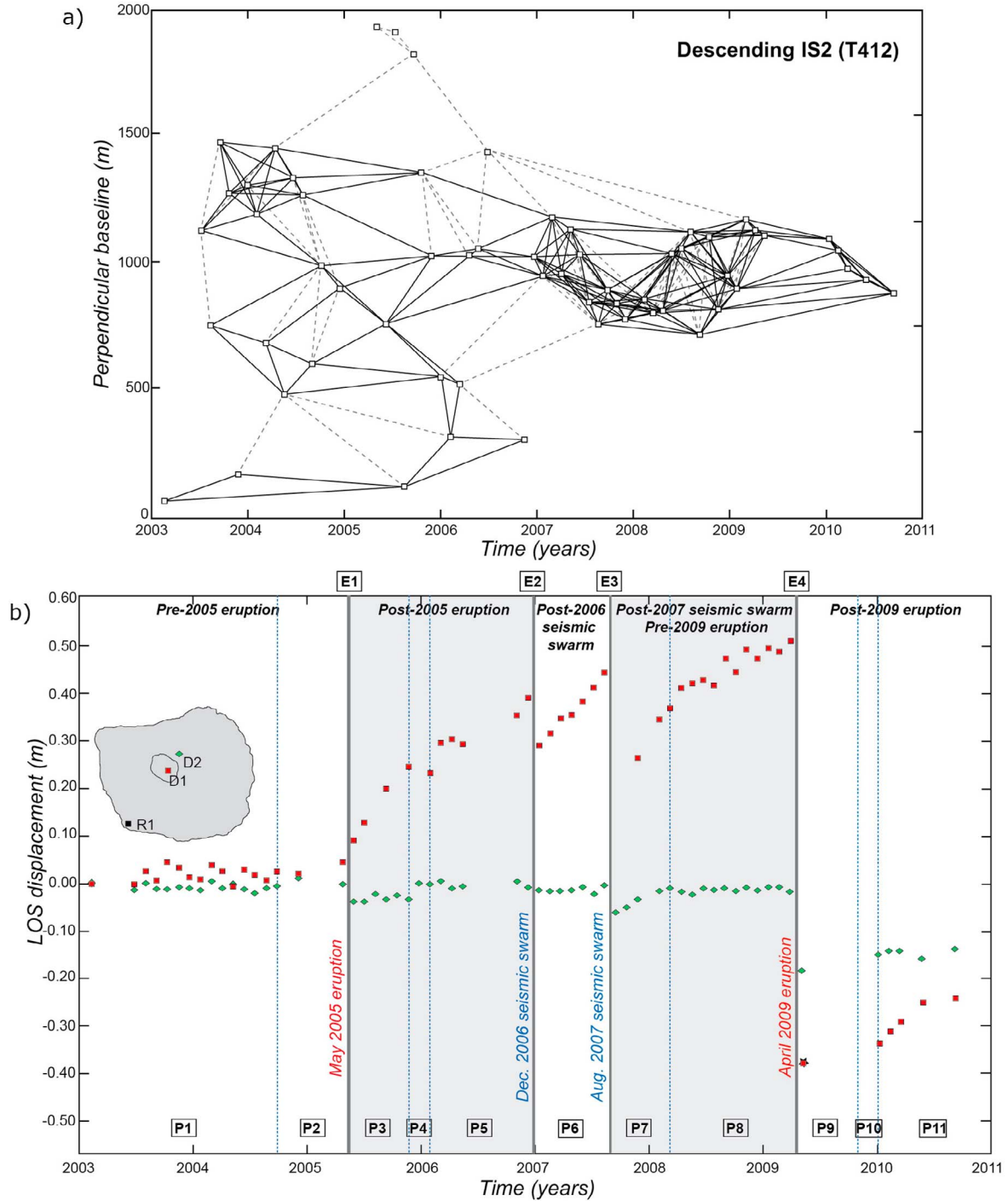


Figure 3. (a) Triangulated network of interferometric pairs used to generate the SBAS time series. Each square represents a SAR acquisition. Solid lines show the selected pairs, dotted lines are pairs that did not meet the selection criteria (see section 3.1). (b) LOS displacement times series relative to R1 for two pixels: (D1) at the center of the summit caldera and (D2) on the northeastern upper flank. Dark gray solid lines represent the occurrence of eruptions or local seismic activity associated to rapid displacement (Event E1–E4). Pre- and post- eruptive/seismic intervals are shown with different background colors. Blue dotted lines represent the occurrence of spatial variations in the deformation pattern and divide the studied interval in eleven time periods (P1 through P11). Red squares and green diamonds mark LOS surface displacement for each location at the time of SAR acquisitions. The intracaldera displacement associated with the 2009 eruption cannot be fully measured using the ENVISAT data set. The total LOS displacement shown here (black star) is obtained from the analysis of SAR data acquired by the L-band ALOS satellite [Baker, 2012].

Table 2. Major Magmatic and Seismic Events Occurring at Fernandina During the Studied Period, Duration and Characteristics

Event	Start Date	End Date	Notes
May 2005 eruption	13 May 2005	29 May 2005	Circumferential fissures on the southern caldera rim
Dec. 2006 seismic swarm	22 December 2006	23 December 2006	2 major shocks, max magnitude m_b 4.0
Aug. 2007 seismic swarm	27 August 2007	30 August 2007	8 major shocks, max magnitude M_w 5.4
April 2009 eruption	10 April 2009	28 April 2009	Radial fissures on the southwestern flank

generated we set a rectangular area of interest (AOI) that encloses most of Fernandina Island and remove those images that have more than 50% of pixels with a coherence value lower than 0.4 within the AOI. With this approach we assess the overall quality of each interferogram and, by removing the images where pixels with low or null coherence prevail, we increase the likelihood for each pixel of maintaining good coherence through time. Several SAR acquisitions are affected by a varying degree of atmospheric water vapor delay, particularly in the summit area, and a few acquisitions present significant noise level due to ionosphere perturbations, frequent in equatorial areas. We therefore evaluate each interferogram and exclude from our selection those SAR acquisitions affected by strong atmospheric and ionospheric perturbations, which could strongly interfere with the deformation signal and generate ambiguity on the source of the phase delay. In a last step we check for missing interconnections in the network and we remove the isolated pairs.

[16] We finally obtain an optimized, high quality (high signal-to-noise ratio) connected network of interferometric pairs (descending IS2, Figure 3a; ascending IS2, Figure S1 in the auxiliary material) and we use the University of Miami-RSMAS InSAR time series software package [Gourmelen *et al.*, 2010] to retrieve the temporal evolution of surface displacement.¹ Each LOS displacement time series is relative to a single pixel that exhibits high coherence and is located in an area where surface deformation is minimum throughout the entire studied-period (descending IS2, R1 in Figure 3b). LOS displacement, along the ground-satellite direction, is considered positive when the offset is toward the satellite and negative when directed away from it.

4. Volcanic Activity and Surface Deformation at Fernandina

4.1. Overview

[17] The analysis of the InSAR time series and of individual interferograms reveals that surface deformation at Fernandina varies both in time and in space. LOS displacement history for the descending pass is presented in Figure 3b. The highest rates of deformation are always recorded at the center of the summit caldera in periods of both inflation and deflation. At this location (D1, red squares) we recognize four major events (E1 through E4) that produce large and rapid (<35 days) displacement and that are directly ascribable to volcanic eruptions or synchronous to local seismic activity (2005 and 2009 eruptions; 2006 and 2007 seismic swarms; gray vertical lines in Figure 3b, details in Table 2). These events divide the entire study period into five intervals that represent pre- or post-eruptive/seismic activity (marked with white or gray background in Figure 3b).

Because of spatial variations of the deformation pattern within each interval we further subdivide them into a total of eleven periods (P1 through P11, details in Table 3), limited by blue-dashed lines in Figure 3b. Since the acquisition of SAR data is not continuous in time but limited by the repeat-pass cycle of the satellite, we are not able to determine the exact occurrence of each change in the deformation pattern. Therefore, we use the time of the closest SAR acquisition to define the start-date and the end-date of each period, with an uncertainty ranging from 13 h to 10 days.

[18] We observe that while intracaldera LOS displacement is always present, there are also short-lived episodes of deformation (<7 months) involving a broader area that widely extends outside the caldera. The LOS displacement time series for a second pixel located on the northeastern upper flank and outside the caldera (D2, green diamonds in Figure 3b) shows the deformation history for this second area.

[19] From the ENVISAT data set we are not able to fully retrieve the intracaldera displacement associated with the April 2009 eruption. In fact, the large deformation results in high fringes rates within the caldera (LOS displacement of half or more the signal wavelength between adjacent pixels) leading to difficulties in the phase unwrapping step and impacting the usability of the differential interferograms in the displacement time series [Casu *et al.*, 2011]. However, a maximum LOS displacement of -0.88 m has been successfully measured by an independent study that uses SAR data acquired by the L-band (operating wavelength of 236.2 mm) Japanese Space Agency's ALOS PALSAR satellite [Baker, 2012]. Therefore, for the entire studied period the net LOS displacement is negative both within the caldera (-0.24 m at its maximum) and in the remaining area around the summit. Rates of intracaldera inflation are variable and maximum values are recorded during P7 (52.1 cm/yr), when deformation occurs both within and outside the caldera.

[20] LOS displacement maps obtained from the SBAS analysis are not shown here due to the large number of pixels that do not maintain coherence during the entire studied period. The occurrence of two eruptions with large displacements, the presence of steep slopes and of patches of vegetation, generate loss of phase coherence in the upper part of the volcano where most of the deformation occurs. We instead present a selection of high signal-to-noise ratio interferograms, from the descending or the ascending IS2 passes, spanning the four major events (Figure 4) and each period (Figure 5). A detailed description of each period and of each major event is given below in chronological order. When available, we provide information relative to the known volcanic activity and to the recorded local seismicity, and correlate such activities to the observed displacement. Earthquake locations (Figure 6) are derived from the U.S. Geological Survey – National Earthquake Information

¹Auxiliary materials are available in the HTML. doi:10.1029/2012JB009465.

Table 3. Time Periods of Surface Deformation at Fernandina Volcano Separated by the Date of the Nearest SAR Acquisition and Type of Activity

Time Period/Event	SAR Acquisition Dates	Deformation Type
Pre-2005 eruption		
Period 1	11 Feb. 2003–28 Sept. 2004	Intracaldera inflation/deflation
Period 2	28 Sept. 2004–7 May 2005	Intracaldera and edifice-wide inflation
2005 eruption		
Event 1	7 May 2005–31 May 2005	Intracaldera and edifice-wide deflation;
Post-2005 eruption		
Period 3	31 May 2005–22 Nov. 2005	Intracaldera inflation
Period 4	22 Nov. 2005–31 Jan. 2006	Intracaldera and edifice-wide inflation
Period 5	31 Jan. 2006–22 Dec. 2006	Intracaldera inflation
December 2006 seismic swarm		
Event 2	22 Dec. 2006–16 Jan. 2007	Intracaldera deflation and minimum edifice-wide deflation; southeastern flank uplift
Post-2006 seismic swarm		
Period 6	16 Jan. 2007–25 Aug. 2007	Intracaldera inflation
August 2007 seismic swarm		
Event 3	25 Aug. 2007–18 Sep. 2007	Intracaldera and edifice-wide deflation; southeastern flank uplift
Post-seismic/pre-2009 eruption		
Period 7	18 Sep. 2007–11 Mar. 2008	Intracaldera and edifice-wide inflation
Period 8	11 Mar. 2008–10 Apr. 2009	Intracaldera inflation
April 2009 eruption		
Event 4	10 Apr. 2008 8 A.M.–5 May 2009	Intracaldera and edifice-wide deflation; uplift of southern caldera rim and eastern side of the eruptive fissures
Post-2009 eruption		
Period 9	5 May 2009–3 Oct. 2009	Intracaldera inflation
Period 10	3 Oct. 2009–1 May 2010	Intracaldera and edifice-wide inflation
Period 11	1 May 2010–18 Sep. 2010	Intracaldera inflation

Center (USGS-NEIC) database and based on data recorded by the Global Seismic Network (GSN). Epicenter locations are affected by varying uncertainties (5–100 km) depending on the earthquake magnitude and the number of stations used to locate the earthquake. The lack of stations close to the western Galápagos Islands results in large location uncertainties (>10 km, Figures S3 and S4 in the auxiliary material) for earthquake of magnitude less than 5.

4.2. Pre-2005 Eruption (P1 and P2)

[21] Our study begins with the first available full-coverage ENVISAT SAR image acquired on 11 February 2003 and the first interval ends with the May 2005 eruption. The first 20 months of this interval form P1, characterized by small LOS displacements (<5 cm) mostly occurring in an area limited by the caldera rim (Figure 5a). Starting from the end of September 2004, intracaldera deformation is associated to displacement of a broader area that extends outside of it and covers the entire summit of the volcano (Figure 5b). Positive LOS displacement characterizes both areas (P2). This pattern of edifice-wide deformation is recorded until the last pre-eruption acquisition.

4.3. The May 2005 Eruption (E1)

[22] On the morning of 13 May 2005, a circumferential eruptive fissure, formed by a set of 5 right-stepping en echelon segments, opened on the southern summit plateau of Fernandina (Figure 2b). The eruption that lasted until 29 May, was preceded by a m_b 5.0 earthquake on 11 May, whose epicenter has been located (USGS-NEIC) ~30 km east of Fernandina's summit (red square in Figure 6).

[23] The interferograms spanning the eruption show: (i) a local area of positive LOS displacement centered on the southern caldera rim, where the circumferential fissure opened, superimposed to (ii) a broad area of negative LOS displacement, that covers a large part of the island (Figure 4a). It is also evident how the emplacement of the lava flows on the southern upper flank causes loss of phase coherence for this area.

4.4. Post-2005 Eruption (P3 Through P5)

[24] Interferograms spanning the post-2005 eruption time interval record a first period characterized by positive LOS displacement only within the caldera, lasting until November 2005 (P3, Figure 5c). From this time through late January 2006, persistent displacement within the caldera is associated with deformation of a larger area similar to the one displaced during the co-eruptive phase (P4, Figure 5d), with both areas showing positive LOS displacement. In February 2006 the edifice-wide deformation ceases and only the caldera continues to show positive LOS displacement until late December 2006 (P5, Figure 5e). Only two months of this eighteen-month-long time interval show edifice-wide deformation, which started with a delay of about six months after the 2005 eruption ended.

4.5. December 2006 Seismic Swarm, Co-seismic (E2) and Post-seismic (P6)

[25] The general trend of re-inflation that characterizes the post-2005 eruption interval is suddenly interrupted in correspondence with the occurrence of seismic activity close to Fernandina Island on 22–23 December 2006 (E2). The USGS-NEIC located two major earthquakes (m_b 4.0 on

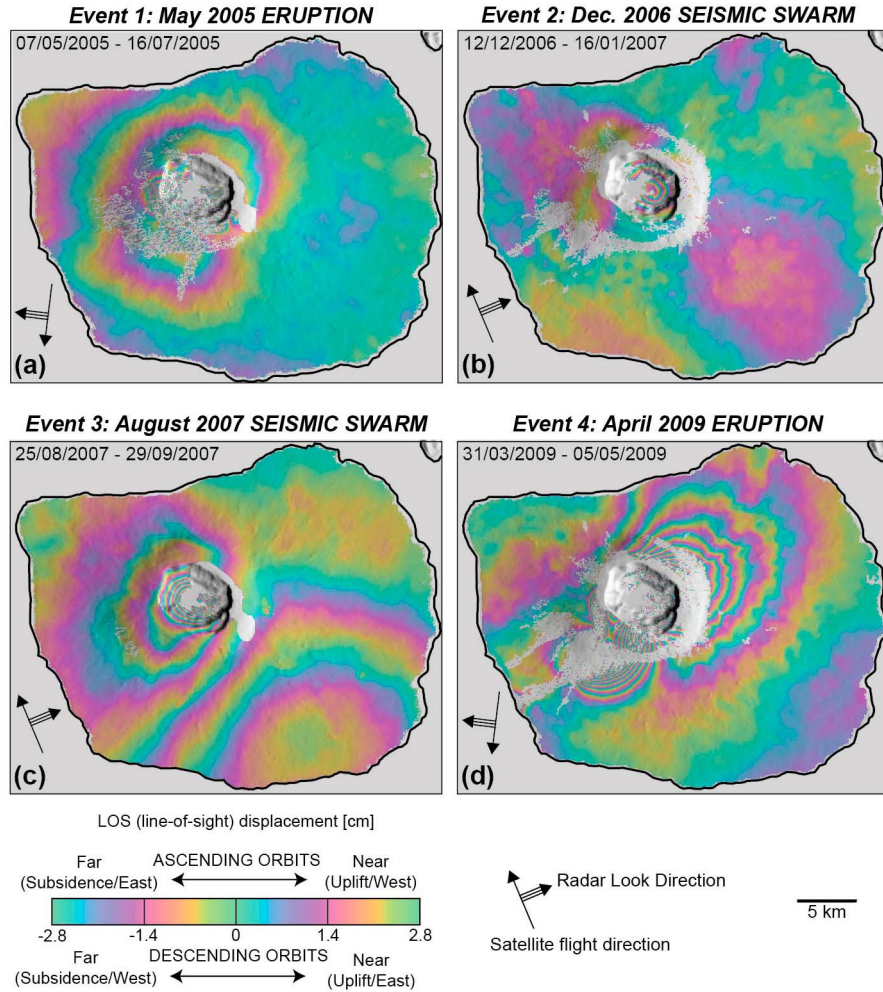


Figure 4. Selection of ENVISAT SAR interferograms showing the surface deformation at Fernandina associated with the four eruptive/seismic events (E1-E4). Detailed information for each event is given in Section 4. Satellite flight direction (ascending T61, descending T412) and radar look direction are presented with arrows. Both tracks are standard beam IS2 (look angle 19.2°–26.7°). Each fringe (full color cycle) represents 2.8 cm of range change between the ground and the satellite, or LOS (line-of-sight) displacement. Areas with low interferometric coherence (<0.3) are uncolored.

22 December and *N/A* on 23 December) within ~85 km of the summit of Fernandina (green squares in Figure 6). Interferograms spanning this event (Figure 4b) show rapid (<35 days) negative LOS displacement of the caldera and of the summit area. While the signal within the caldera is well defined (~−0.09 m at its maximum) it is subtler for the rest of summit area (<0.03 m). The same interferograms also reveal a broad area of positive LOS displacement on the southern flank of the volcano. No eruptive activity was detected.

[26] Information on the timing between the occurrence of the seismicity and the associated surface deformation can be obtained from a SAR image acquired between the two main shocks, 6 h after the occurrence of the first earthquake. In interferograms generated using this image there is no evidence of the deformation observed in later acquisitions. The total displacement is however present in the following SAR

image acquired five days later, on 28 December 2006 (see Table S1 and Figures S2a and S2b in the auxiliary material).

[27] Surface deformation following the December 2006 seismic swarm is characterized by intracaldera positive LOS displacement only (~0.15 m at its maximum) with a pattern similar to previous periods of intracaldera uplift (P6, Figure 5f). Further seismic activity occurred on 5 February 2007, in the same area of the previous seismic events (m_b 4.1, blue square in Figure 6), but in this case there is no clear evidence of perturbations in the pattern of deformation at Fernandina. The positive LOS displacement within the caldera is detected until late August 2007.

4.6. August 2007 Seismic Swarm (E3)

[28] Between 27 August and 30 August 2007, the GSN recorded 8 major earthquakes in the vicinity of the Galápagos archipelago with magnitudes (M_w or m_b) between 3.8 and 5.4 (USGS-NEIC). Epicenters for five main shocks are

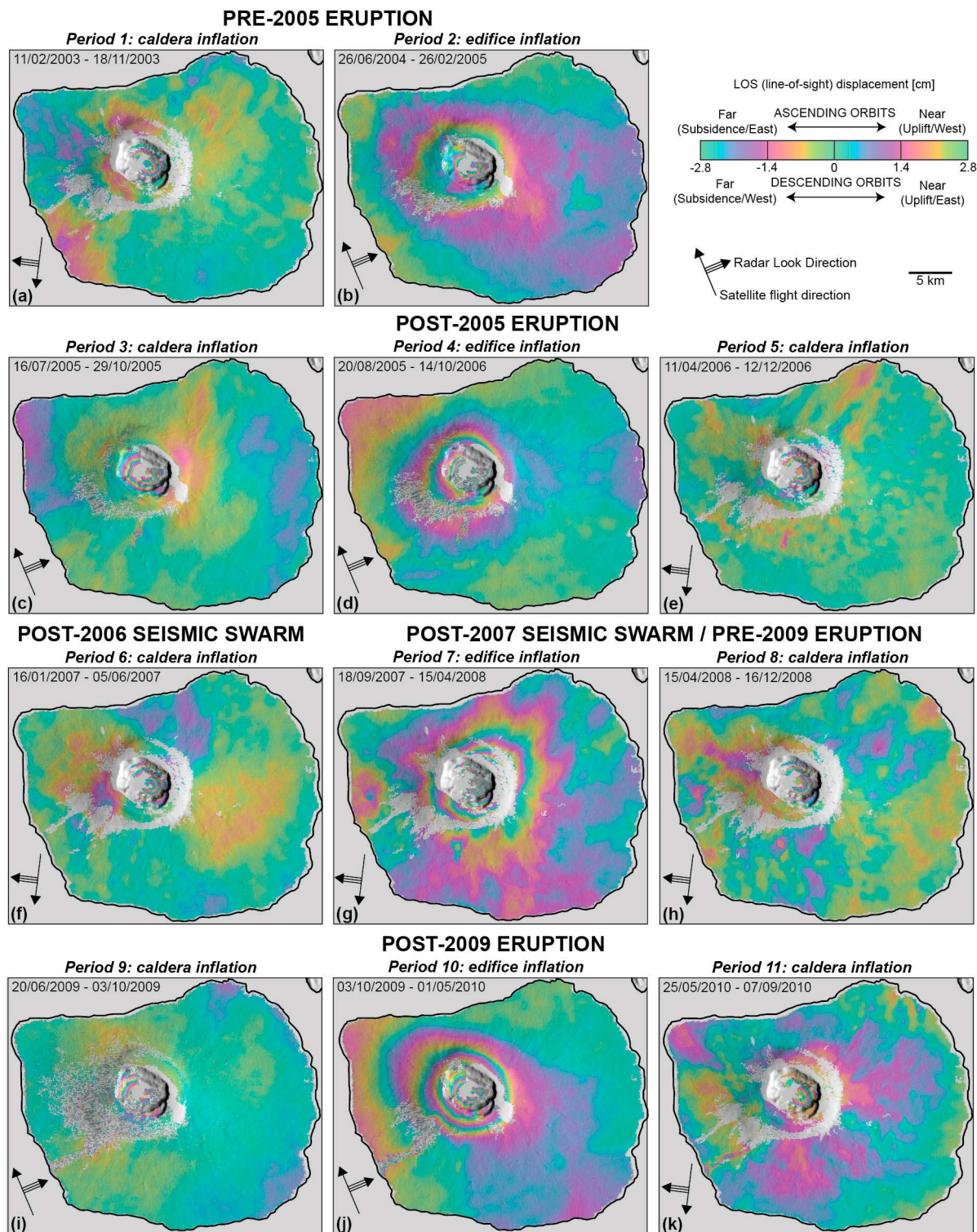


Figure 5. Selection of ENVISAT SAR interferograms showing spatial variations in the surface deformation at Fernandina associated with periods of inflation (P1-P11). (left and right) Periods of deformation within the caldera only and (middle) periods of edifice-wide displacement. Detailed information for each period is given in Section 4. Satellite flight direction (ascending T61, descending T412) and radar look direction are presented with arrows. Both tracks are standard beam IS2 (look angle 19.2°–26.7°). Each fringe (full color cycle) represents 2.8 cm of range change between the ground and the satellite, or LOS (line-of-sight) displacement. Areas with low interferometric coherence (<0.3) are uncolored.

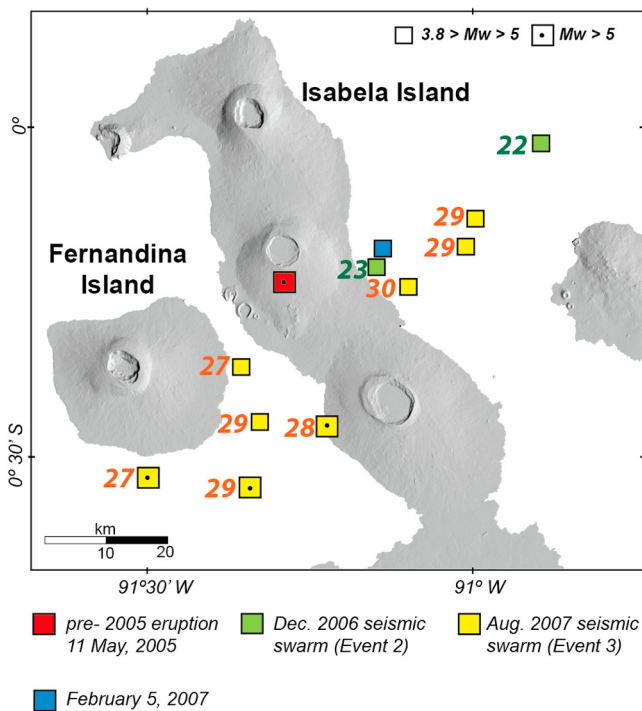


Figure 6. Map of the seismicity in the western Galápagos Islands during the studied period. Squares represent the location of major seismic events recorded by the global seismic network, retrieved from the USGS/NEC PDE Catalog. For the two seismic swarms the numbers indicate the days of the month.

located within 35 km of the summit of Fernandina and the rest of the events within 60 km (yellow squares in Figure 6). A large location uncertainty is associated with the lower magnitude earthquakes and the linear pattern formed by the epicenters suggests the presence of artifacts in the estimated locations.

[29] All the interferograms that entirely span the August 2007 seismic swarm show a very distinctive pattern of deformation: (i) the caldera and the summit area show up to -0.36 m of LOS displacement, while (ii) a broad area located on the southern flank of Fernandina, similar to the one displaced during the December 2006 seismic swarm, shows up to 0.06 m of positive LOS displacement (Figure 4c). By looking at the geometry of the interferometric fringes on the southern flank we can infer that a large portion of the uplifting area lies below sea level, where InSAR does not provide any measurements. However, no deformation is detected on the nearby Isabela Island and no surface or submarine eruptions have been reported.

[30] Two SAR images acquired during the seismic swarm provide further information on the timing between seismicity and surface deformation. On 28 August 2007 (SAR image from T104), ~ 8 h after the first earthquake and between the second and the third major shocks, there is already evidence of surface deformation involving large part of the island, but its magnitude is only a portion of the total displacement recorded by later acquisitions. Interferograms formed using the following SAR image acquired on 30 August (T61), ~ 9 h after the last recorded

earthquake, show the entire displacement associated with this event (see Table S2 and Figures S2c and S2d in the auxiliary material).

4.7. Post-2007 Seismic Swarm and Pre-2009 Eruption (P7 and P8)

[31] Interferograms spanning the early post-seismic interval reveal positive LOS displacement in both areas, within the caldera and across the broad area that showed subsidence during the previous event (P7, Figure 5g). Also in this case the LOS displacement rate is larger within the caldera. No displacement is detected for the southern lower flank of Fernandina that showed uplift during the seismic swarm. This pattern of deformation is recorded for about six months, until March 2008. Interferograms generated using SAR images acquired during or after April 2008 do not show any displacement outside the caldera (P8, Figure 5h).

4.8. The April 2009 Eruption (E4)

[32] During the night between 10 and 11 April 2009, a new eruption started at Fernandina Volcano: three main radial fissures (Figure 2b) opened on the southwestern flank and produced lava flows that reached the ocean [Bourquin et al., 2009]. The eruption ended on 28 April. Two areas of positive LOS displacement, one centered on the southwestern caldera rim and one on the eastern side of the eruptive fissures, represent the surface expression of the propagation of the feeding dike and the opening of the eruptive fissures (Figure 4d). As for the previous eruption and for the deformation associated with the seismic swarms, the caldera and a large portion of the island show negative LOS displacement. The subsiding area outside the caldera is similar to the one displaced during previous episodes as for shape and gradient variations of the interferometric fringes.

4.9. Post-2009 Eruption (P9 Through P11)

[33] The last interval studied here spans sixteen months after the April 2009 eruption, with the last SAR acquisition acquired on 18 September 2010. From November 2010 the ENVISAT satellite changed its orbit and interferograms between images acquired before and after this date are no longer possible.

[34] As during the post-eruptive interval that followed the 2005 eruption, the early post-2009 eruption interval (P9) is characterized by rapid positive LOS displacement only within the caldera (Figure 5i). After five months from the end of the eruption, beginning in October 2009, the InSAR data record edifice-wide positive LOS displacement (P10, Figure 5j). This pattern of deformation persists for more than seven months until May 2010, when positive LOS displacement only within the caldera characterizes the remaining four months of the study period (P11, Figure 5k).

5. Sources of Deformation and Modeling

5.1. Active Sources of Deformation

[35] The analysis of the InSAR data reveals the presence of multiple sources of deformation active at different times and locations, implying the existence of a complex magmatic plexus rather than a system formed by a single magma chamber. Two recurrent patterns of deformation are centered

Table 4. Results From Nonlinear Inversion of InSAR Data: Estimated Source Parameters for the Shallower Source (Horizontal Sill), the Deeper Source (Oblate Spheroid) and the August 2007 Intrusion (Horizontal Sill)^a

Length (km)	Width (km)	Depth (km)	Latitude	Longitude	Strike (deg)	Opening (m)	Volume Change (10^6 m^3)
<i>Shallower Source^b</i>							
2.8 [2.43–3.15]	2.03 [1.60–2.45]	1.08 [0.81–1.34]	0.3795 S ^c	91.5504 W ^c	121° [108°–135°]	0.2 [0.14–0.26]	1.1
<i>a</i>							
<i>b/a</i>							
2.73 [1.96–3.70]	0.18 [0.11–0.30]	4.93 [4.32–5.58]	0.3684 S ^c	91.5466 W ^c	48° [26°–67°]	$7.45*10^{-3}$ ^e [$3.30*10^{-3}$ – $9.89*10^{-3}$]	
<i>Deeper Source^d</i>							
<i>Length (km)</i>							
<i>Width (km)</i>							
<i>Depth (km)</i>							
<i>Latitude</i>							
<i>Longitude</i>							
<i>Strike (deg)</i>							
<i>Normalized Pressure Change (μPa)</i>							
<i>August 2007 Intrusion^f</i>							
17.55 [15.86–19.39]	21.7 [14.24–29.57]	4.49 [3.60–5.52]	0.4227 S ^c	91.4974 W ^c	222° [fixed]	0.05 ^e [0.04–0.06]	19

^aThe 95% confidence intervals are shown in brackets. RMS – root mean square. Sill dip angle is fixed to 0°. Oblate spheroid dip angle is fixed to 0°.

^bAscending IS2 (27/01/2007–21/07/2007), descending IS7 (26/01/2007–20/07/2007), and RMS = 9.52 mm.

^cMean.

^dAscending IS2 (29/09/2007–26/04/2008), descending IS7 (28/09/2007–25/04/2008), and RMS = 6.31 mm.

^eFor $\mu = 5 \text{ GPa}$ $\Delta V = 15.4 \cdot 10^6 \text{ m}^3$ [Tiampo et al., 2000].

^fAscending IS2 (25/08/2007–29/09/2007), descending IS7 (24/08/2007–28/09/2007), and RMS = 23.63 mm.

at the summit caldera but have different areal extensions. They are interpreted as the expression of variations in the excess fluid pressure in two long-term magma reservoirs located at different depths. A relatively shallow source produces almost continuous displacement within the caldera. A second, deeper one is intermittently active and produces edifice-wide displacement. Additional sources of deformation are active during the two seismic swarms (E2 and E3) and the two eruptions (E1 and E4). During the two seismic swarms the deformation on the southern flank is generated by a relatively deep source (given the low gradient of the interferometric fringes), likely representing the lateral intrusion of magmatic bodies. The two eruptions show deformation associated with the shallow intrusion of the eruptive dikes together with deflation of the entire summit of the volcano [Chadwick et al., 2011].

5.2. Modeling Approach

[36] Among the different sources of deformation active during the studied period we model the two interpreted as magma reservoirs, and the intrusion associated with the August 2007 seismic swarm (E3). The model for E3 can be representative for the other seismic swarm/intrusion (E2) for which the measured surface displacement is too small for a robust estimation of the source parameters. The geometry of eruptive dikes feeding the eruptions (E1 and E4) is very complex [e.g., Chadwick et al., 2011] and since it is not considered fundamental for this study is not modeled here. Our modeling strategy is as follow: we identify, for the three sources, the interferograms with the highest signal-to-noise ratio within periods for which contemporary ascending and descending interferograms (descending SAR image acquired ~ 13 h before the ascending one) are available. We then perform a nonlinear inversion of the InSAR data in a homogeneous isotropic elastic half-space. Magma bodies are modeled as rectangular dislocation sources with uniform opening [Okada, 1992] or as fluid-pressurized ellipsoidal cavities [Yang et al., 1988]. We also tested for point sources [Mogi, 1958] and other radially symmetric cavities [e.g.,

McTigue, 1987; Fialko et al., 2001] but the modeled surface deformation of these sources did not fit the data well, indicating the necessity for more complex geometries. In all models we assume a Poisson's ratio $v = 0.25$ for the elastic half-space. Since each full-resolution SAR interferogram subset for Fernandina consists of about 10^7 data points, we perform spatial averaging using the *Quadtree* algorithm [Jónsson et al., 2002]. The reduced data sets consist of a minimum of 503 and a maximum of 920 data points. For each data set we determine best fit source parameters such as location (x, y, z), geometry (length l and width w , or major axis a and aspect ratio b/a), strength (opening or normalized excess pressure $\Delta P/\mu$) from expressions given by Okada [1992] and Yang et al. [1988] respectively. Unit variance is assumed for all data points. To evaluate the quality of the predicted deformation we use the normalized root-mean square error (RMSE) between observed and modeled interferograms, defined as:

$$\text{RMSE} = \sqrt{\frac{1}{N} \sum_{i=1}^N (d_i - m_i)^2}$$

where d is the data, m is the model prediction, and N is the number of data points. We estimate the optimal solution together with the posterior probability density distributions of the parameters, as indicators of resolution and uncertainties, using the Monte-Carlo based Gibbs sampling (GS) algorithm [Brooks and Frazer, 2005].

[37] The effect of topography on the surface deformation signal is taken into account using the approach proposed by Williams and Wadge [1998]. The varying depth model corrects the changing distance between the source and the surface by varying its depth with topography.

5.3. Results

[38] We first model the most active source of deformation, which generates displacement within the caldera. The most

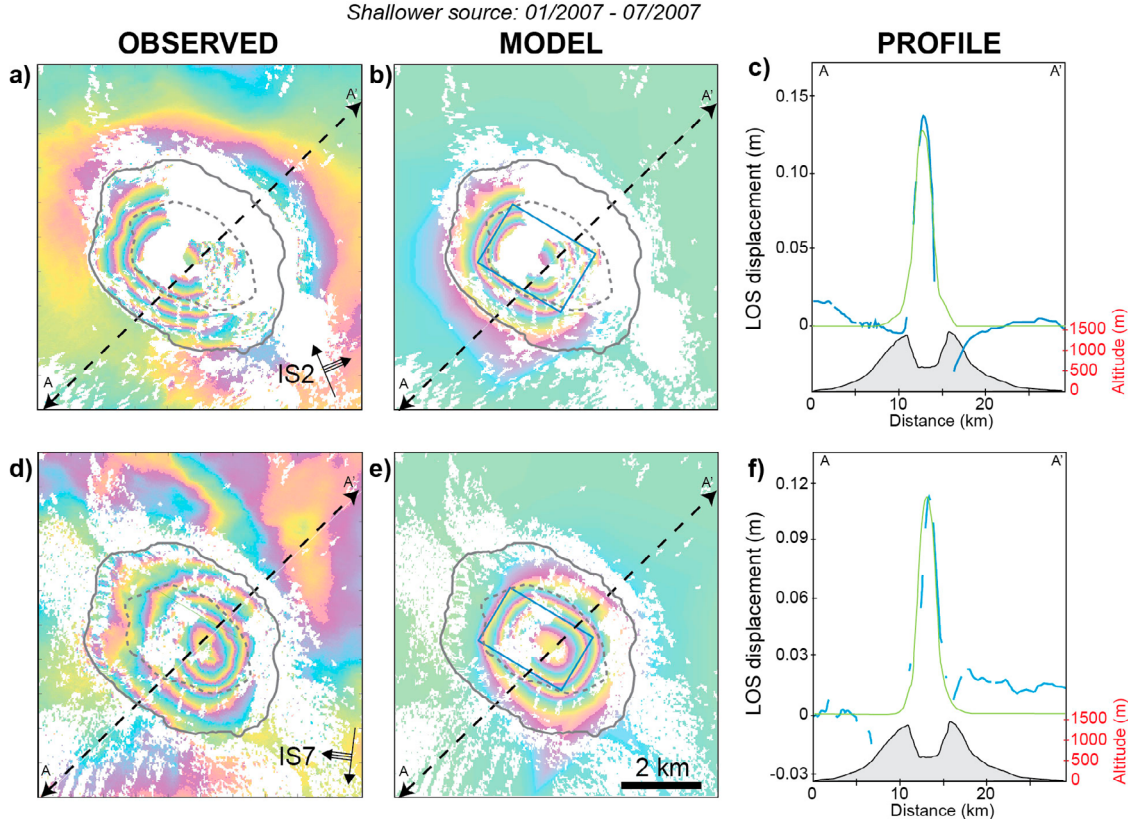


Figure 7. Modeling results for the shallower source: (a and b) ascending IS2 and (d and e) descending IS7, comparison between observed data and model predictions. (c and f) Comparison between topography (in gray), observed (in blue) and modeled (in green) surface displacement along the A-A' trace (see Figure 8). Surface deformation is modeled using a rectangular horizontal sill (blue rectangle). For source parameters see Table 4. The solid and the dashed gray lines represent the summit caldera rim and the caldera floor outline respectively.

suitable data set spans 175 days within P6 (specific dates are reported in Table 4). We invert for a horizontal, uniform opening dislocation source, representing the top surface of a sill-like shallow magma reservoir. We fix the sill to be horizontal while all the other parameters are allowed to float within geologically realistic values. The best fitting model centers the sill beneath the caldera at a depth of ~ 1.1 km below sea level (~ 1.6 km below the caldera floor), within a 95% confidence interval ranging from 0.8 to 1.3 km. The inferred sill is ~ 2.8 km long and ~ 2.0 km wide, and oriented NW-SE. The comparison between the observed InSAR data and the predicted LOS displacement shows good agreement for both viewing geometries (Figures 7a–7f).

[39] We next model the second, deeper source, for which deformation extends outside the caldera. The LOS displacement during periods of edifice-wide deformation shows only one maximum at the center of the caldera and decreases radially away from the summit. However, the radial decrease is not regular and shows a significant gradient contrast between the area inside the caldera and the rest of the summit. Therefore, the displacement field cannot be explained by a single source. We model it as a stack of two sources but given the difficulty of modeling their contemporary contributions, we mask out the deformation inside the caldera and invert the remaining data for a deeper source only. We

find that an oblate spheroid cavity provides a better fit than a uniform opening dislocation source. The inversion is performed using two interferograms spanning 210 days within P7, when edifice-wide deformation is recorded and there is no evidence for further active sources other than the two centered below the summit. The best fitting oblate spheroid is centered beneath the summit at a depth of ~ 4.9 km b.s.l. (95% confidence interval: 4.3–5.6 km) with the ~ 2.7 km long major axes a oriented in the NE-SW direction (azimuth of 48 degrees from north). We then reintroduce the data points previously masked and, by fixing the geometries of both sources and the inferred normalized excess pressure for the deeper one, we invert for the opening of the shallower source only. Our model is able to well reproduce the LOS displacement, in particular for the ascending IS2 viewing geometry (Figures 8a–8f).

[40] A third model is generated to reproduce the uplift of the southeastern flank associated with E3. In this case, we invert ascending and descending 35-day interferograms spanning the event. For simplicity we fix the geometries and the positions of the two sources previously inferred and invert for a further planar dislocation source with uniform opening. Best fit is obtained for a $\sim 17.5 \times \sim 21.7$ km horizontal rectangular sill, located at a depth of ~ 4.5 km b.s.l. (95% confidence interval: 3.6–5.5 km) and a total volume of

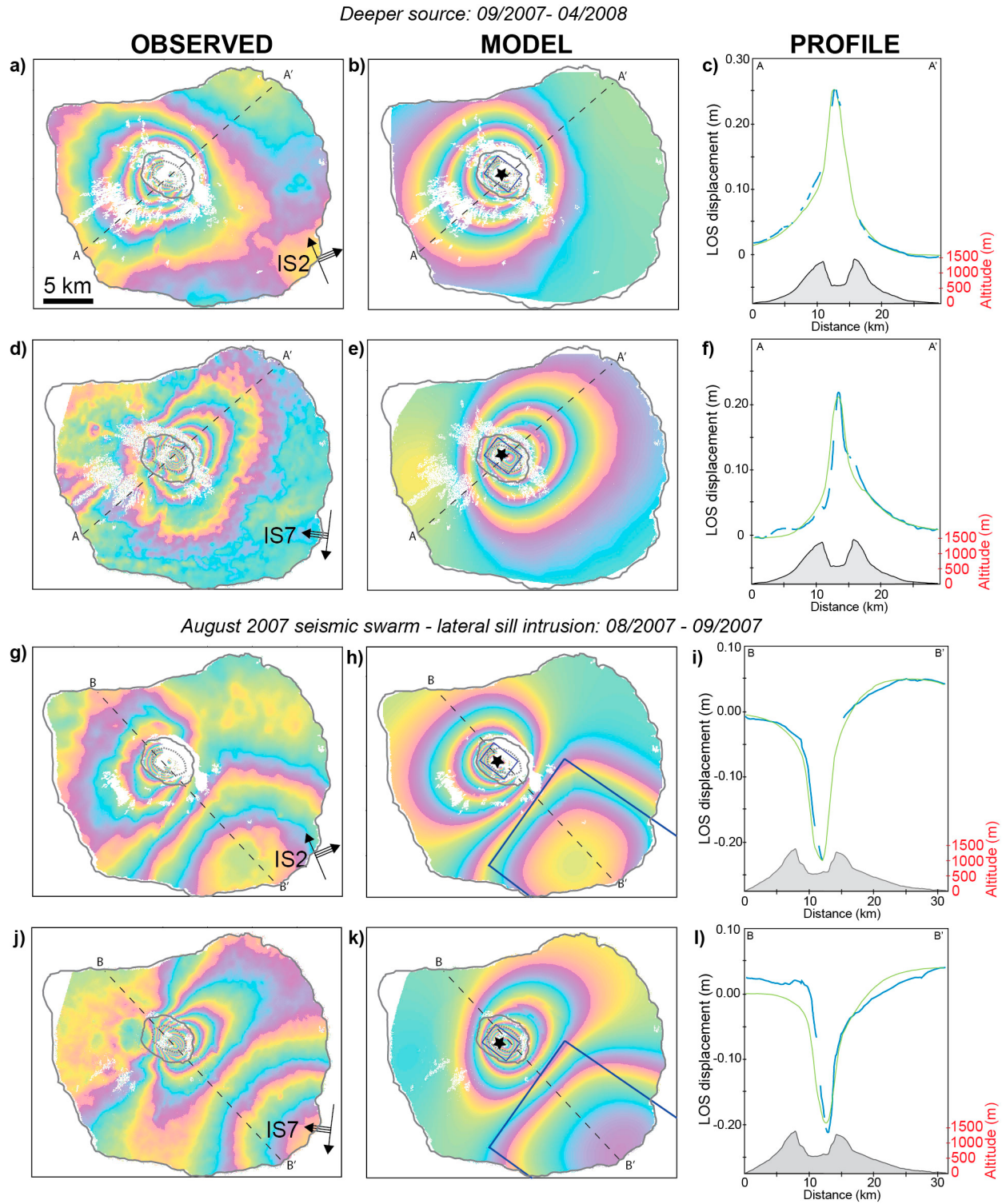


Figure 8. Modeling results: deeper source, (a and b) ascending IS2 and (d and e) descending IS7, and August 2007 lateral sill intrusion, (g and h) ascending IS2 and (j and k) descending IS7, comparison between observed data and model predictions. (c, f, i, and l) Comparison between topography (in gray), observed (in blue) and modeled (in green) surface displacement along the A-A' and the B'B' traces. Surface deformation is modeled using an oblate spheroid for the deeper source (black star), and rectangular sills for the shallower source and the August 2007 intrusion (gray and blue rectangle respectively). For source parameters see Table 4. The solid and the dashed gray lines represent the coastline of Fernandina Island, the summit caldera rim and the caldera floor outline respectively.

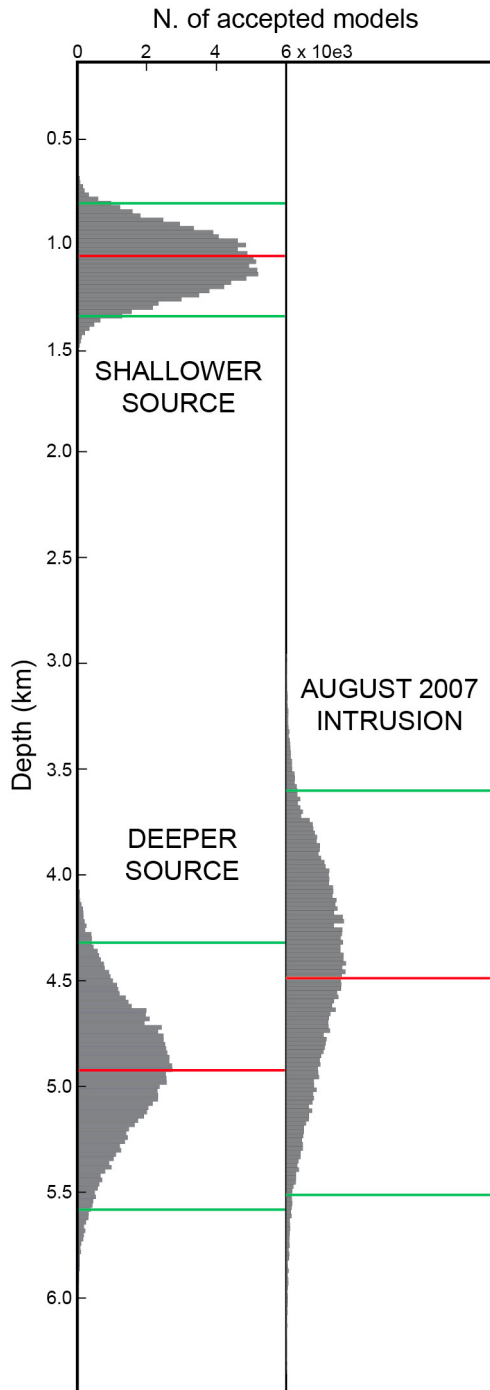


Figure 9. Normalized posterior probability distributions for the depth parameter of each source obtained using the Gibbs Sampling algorithm (100,000 samples). Red lines represent the depth of the best fitting models and green lines represent the 95% confidence interval of the modeled parameter.

the intrusion of $\sim 19.0 \times 10^6 \text{ m}^3$. Also in this case, the inferred model is able to largely explain the observed LOS displacement, in particular for the ascending data set (Figures 8g–8l).

[41] A summary with all the modeled source parameters and their 95% confidence interval is presented in Table 4.

The comparison between the normalized distributions for the depth of each source clearly shows the depth difference between the two magma reservoirs, and the proximity between the deeper one and the sill intruded during E3 (Figure 9).

6. Discussion

6.1. Implications for the Shallow Magma Storage System

6.1.1. Two Magma Reservoirs

[42] Our analysis indicates the presence of two stacked crustal magma reservoirs beneath the summit of the volcano. We model a shallow flat-topped reservoir at $\sim 1.1 \text{ km}$ b.s.l. overlaying a second, deeper area of magma storage centered at $\sim 4.9 \text{ km}$ b.s.l. Figure 10 shows a schematic cross section of the volcanic edifice and of the upper crust below Fernandina. The total crustal thickness at Fernandina is $\sim 12\text{--}14 \text{ km}$ [Feighner and Richards, 1994]. The lower 6 km represent the pre-existing oceanic crust, locally flexed by the weight of the volcanic edifice, while the upper 6–8 km are the product of the hot spot volcanic activity. The modeled source depths are well constrained and center both reservoirs within the volcanic pile. However, inhomogeneity in the medium elastic parameters, different rheologies (e.g., viscoelasticity) and the presence of discontinuities in the volcanic edifice can significantly affect ground deformation [De Natale and Pingue, 1996] and cause bias of the modeled parameters. In particular, homogeneous elastic models underestimate magma reservoirs depths and volume changes [Montgomery-Brown et al., 2009; Foroozan et al., 2010]. Therefore, the inferred depths would be larger if a layered heterogeneous medium (e.g., with variable Young's modulus) is considered [Manconi et al., 2007] and would center the deeper reservoir at greater depth, likely at the boundary between the volcanic pile and the underlying oceanic crust. Furthermore, if we consider the effect of viscoelastic relaxation within the regions surrounding the magma reservoirs, the estimated source size could be larger [Segall, 2010].

[43] Source modeling is presented here only for specific periods. The remaining periods have similar patterns of deformation, indicating that the same sources are activated during different times and therefore represent permanent areas of magma storage. The surface deformation observed at Fernandina has clear magmatic origin. Evidence is provided by the high eruptive frequency during the recent history and the observation of inter-eruptive uplift and co/post-eruptive subsidence. In Figure 11 we summarize the activity of the two magma reservoirs during each event and period (E1–E4, P1–P11). Excess magma pressure decrease within the reservoirs (expressed by subsidence at the surface) is marked in blue. Its increase (uplift) is marked in red.

[44] Our finding of two shallow magmatic sources is consistent with the model of the 2005 eruption and its pre- and post-eruptive phases of Chadwick et al. [2011], who inferred a shallow sill at $\sim 1 \text{ km}$ below the surface and a deeper point source at $\sim 5 \text{ km}$ depth. Geist et al. [2006a] also modeled GPS and micro-gravity measurements carried out at Fernandina between 2000 and 2002. They inferred the presence of a single source centered under the caldera at a depth of 1.0 km below the surface, which is likely the same as our shallower source. The presence of the second

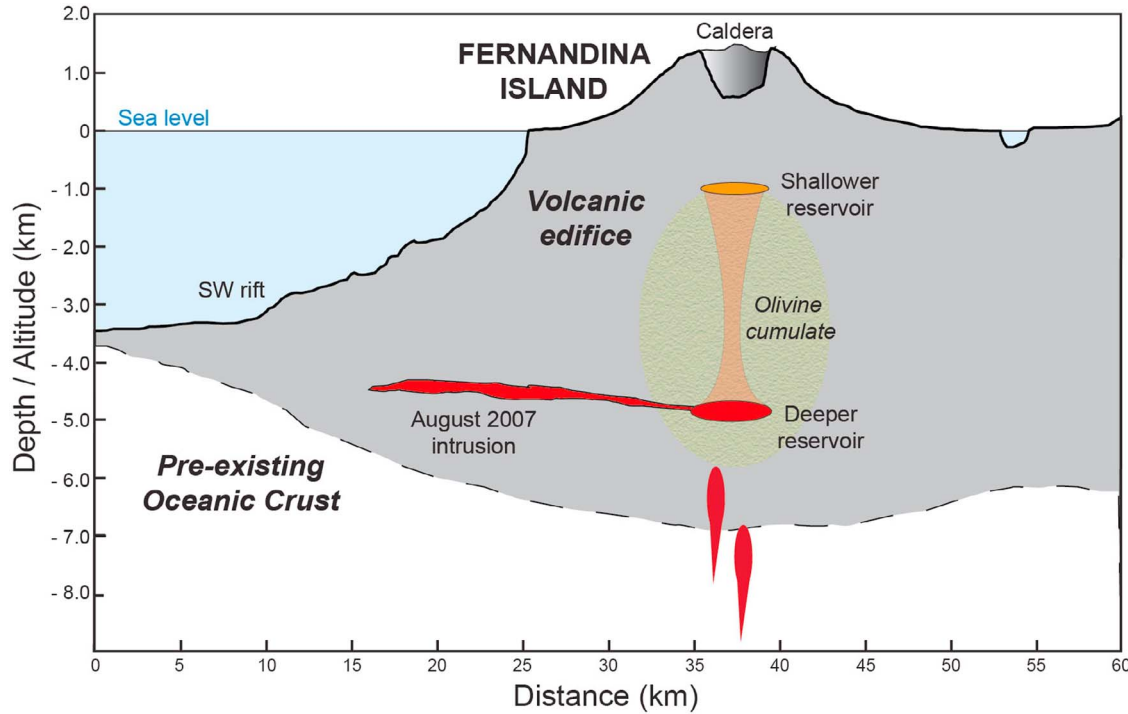


Figure 10. Schematic cross-section across Fernandina Islands and the underlying oceanic crust showing the inferred structure of the shallow magmatic system. Source positions are inferred from the analysis of the InSAR data. The inferred source depths could be larger if a layered heterogeneous medium is considered [Manconi et al., 2007]. For example, the deeper reservoir could likely be centered at the boundary between the volcanic edifice and the underlying oceanic crust. Similarly, the August 2007 intrusion could have propagated along the same boundary.

reservoir was probably missed because of the limited extension of the GPS network.

6.1.2. Comparison With Petrologic Results

[45] Support for our model of two different magma reservoirs at crustal depths is also provided by the petrology of the erupted lavas. Subaerial lavas erupted at Fernandina are monotonous, evolved (plagioclase-dominated mineralogy), and incompatible-element enriched tholeiites. The phase assemblage suggests eruptive temperatures of $\sim 1150^{\circ}\text{C}$ and

is stable only at low pressure ($<0.1 \text{ GPa}$), corresponding to depths of a few kilometers or less [Allan and Simkin, 2000; Geist et al., 2006b]. This is consistent with what we infer for the shallower source ($\sim 1.1 \text{ km b.s.l.}$). The lack of primitive melts within the subaerial lavas suggests extensive mixing and homogenization of evolved melts in a shallow reservoir, testified by the narrow compositional range of the lavas. Allan and Simkin [2000] proposed that this reservoir would

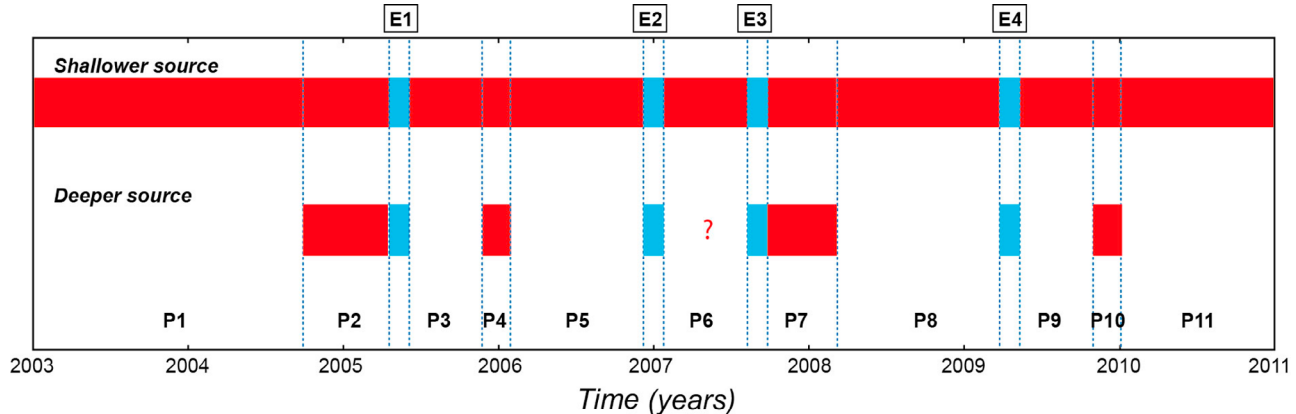


Figure 11. Summary of the activity of the two magma reservoirs during the studied period. The red color represents inflation of the source and uplift at the surface, in blue deflation and subsidence. Dotted blue lines separate the entire interval into 11 time periods of inflation (P1-P11) and 4 events of deflation (E1-E4).

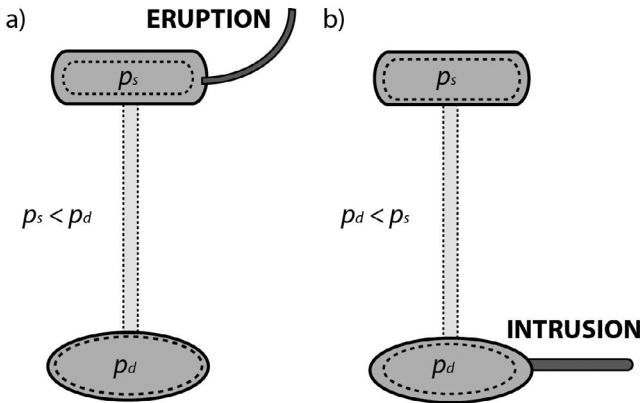


Figure 12. Schematic representation of the excess pressure within the two reservoirs after (a) eruptions and (b) deep intrusions. p_s – excess pressure in the shallower reservoir. p_d – excess pressure in the deeper reservoir.

act as a buffer for magma coming from depth and prevent the eruption of any more primitive melts.

[46] Even if most of submarine lavas erupted at Fernandina are similar in composition to the subaerial suite, *Geist et al.* [2006b] identified two other suites of lava in the submarine record. Evolved basalts and icelandites have been recovered from the SW rift. It is believed that these lavas crystallize and fractionate at pressures between 0.3 and 0.5 GPa, and depths of 10–15 km, greater than any inferred depth for the sources generating the observed surface displacement. These lavas are thought to represent extensive fractional crystallization in the upper mantle and lower crust that would bypass the shallow plumbing system. A second suite, defined as “High-K” lavas and also recovered from the SW rift, is considered as hybridization between the most common series basalts and the evolved series magma. Results from our models could suggest that magma from this last suite is temporarily stored in the deeper reservoir (~4.9 km b.s.l.) and, when subvolcanic lateral intrusions occur and intersect the submarine surface of the volcano, it erupts at the SW rift. In fact, in our model for E3, the sill intrudes toward the southern portion of the volcano at a depth of ~4.5 km b.s.l., close to the area of magma storage inferred for the deeper source.

6.2. Implications for the Shallow Magma Plumbing System

6.2.1. Hydraulically Connected System

[47] We observe that while the shallower source is overall always active (Figure 11), the deeper one generates displacement only during the four events (E1-E4) and during some periods (P2, P4, P7 and P10). During these events and periods, ground deformation and excess pressure have always the same signature in both, the shallower and the deeper reservoirs, either positive or negative. This can be interpreted as evidence for a hydraulically connected system between the two reservoirs. Magma seems to easily migrate from the deeper to the shallower reservoir and vice versa, as shown by contemporary rapid excess pressure variations within both reservoirs.

6.2.2. Dynamics of Magma Migration

[48] A previous study has shown that the dike feeding the 2005 eruption likely originated from the shallower reservoir [*Chadwick et al.*, 2011]. The measured LOS displacement for the 2009 eruption is very similar to the 1995 one for which a shallow dipping dike, extending from the surface to a maximum depth of ~1.3 km, has been inferred [*Jónsson et al.*, 1999]. It is likely that during most eruptions, magma mainly withdraws from the shallower portion of the magma storage system, as also demonstrated by the monotonous petrology of the erupted lavas. An opposite mechanism, with magma withdrawing primarily from greater depth, is suggested by our model for the 2007 subvolcanic intrusion.

[49] The periods of reservoir re-filling and excess magma pressure increase provide further insight into magma migration dynamics. The temporal sequence of surface deformation is different following eruptions than following subvolcanic lateral intrusions. Following eruptions (E1 and E4) first the shallower reservoir inflates for a period of four to six months (P3 and P9), then the two reservoirs inflate contemporarily (P4 and P10) and finally only the shallower source inflates (P5 and P11). The pattern is different after subvolcanic lateral intrusions. Following the larger intrusion (E3), both sources inflate contemporarily (P7) for a seven-month period. Following the smaller intrusion (E2), the shallower reservoir clearly inflates, whereas changes of the deeper source are not resolved (P6).

[50] We explain these observations in terms of (i) temporal variations in excess pressure in the two reservoirs as consequence of eruptions and subvolcanic intrusions (Figure 12), and (ii) differences in magma source stiffness and compliance. Magma reservoirs shaped as ellipsoidal cavities are relatively stiff, whereas cracks (dikes and sills) are highly compliant [*Rivalta and Segall, 2008; Rivalta, 2010*]. For the same amount of excess pressure a compliant source will expand more than a stiff source. However, our interpretation does not include effects from the compressibility of the fluid contained in the reservoirs. We also limit our analysis to fully elastic models, although the presence of viscoelastic rinds surrounding active magma chambers [e.g., *Del Negro et al.*, 2009; *Masterlark et al.*, 2010] or viscous resistance within the conduit connecting the reservoirs could represent further controlling factors on the observed deformation.

[51] Prior to eruptions, we assume equilibrium between the shallower and the deeper reservoirs with identical magma excess pressures, $p_s = p_d$, where p_s and p_d are the excess pressures within the shallower and deeper reservoirs, respectively. An eruption primarily fed by the shallower reservoir is associated with a larger decrease in excess pressure of the shallower than of the deeper reservoir, and after the eruption we have $p_s < p_d$. This pressure gradient would drive newly injected magma toward the shallower reservoir, and inflate it. When excess magma pressure equilibrium is reached ($p_s = p_d$), the pressure gradient to the deep roots of the plumbing system would drive additional magma into the shallow system and both sources would inflate contemporarily. When a threshold is reached, inflation of the deeper reservoir ceases. We interpret this cessation as the consequence of limited source compliance (ellipsoidal cavity). The deeper source cannot further expand and excess pressure increase within the system is primarily accommodated by the inflation of the shallower reservoir. Similarly, a subvolcanic lateral intrusion primarily fed by the

deeper reservoir is associated with a larger decrease in excess pressure of the deeper than of the shallower reservoir. After the intrusion we have $p_d < p_s$. In this case the pressure gradient would drive new magma primarily into the deeper reservoir. We would expect inflation of the deeper reservoir only, but we observe contemporaneous inflation of both sources. We interpret the inflation of the shallower reservoir as the result of the high compliance of this sill-type reservoir. A small increase in excess pressure results in significant inflation of this reservoir. In the same way as following eruptions, once the threshold is reached inflation of the deeper reservoir ceases.

6.3. Subvolcanic Lateral Intrusions and Implications for Caldera Dynamics

[52] The December 2006 (E2) and August 2007 (E3) events represent evidence for subvolcanic lateral intrusions at Fernandina. Even if the 1927 Punta Espinoza rapid uplift and the 1954 Urvina Bay event suggested the occurrence of subvolcanic intrusions at Fernandina and at the other Galápagos volcanoes, such deformation has never been directly measured. Our data provide evidence for the rapid intrusion of relatively large volumes of magma at depth (e.g., $\sim 0.02 \text{ km}^3$ in August 2007), comparable with intruded and erupted volumes associated with the previous eruptions (e.g., 1995 eruption, $\sim 0.05 \text{ km}^3$ [Jónsson *et al.*, 1999; Rowland *et al.*, 2003] and 2005 eruption, $\sim 0.026 \text{ km}^3$ [Chadwick *et al.*, 2011]). Furthermore, we can speculate that similar events might have occurred in the recent history of the volcano, but gone unnoticed because of less dramatic uplift. These intrusions could also represent an important mechanism for the growth of the volcanic edifice and the surrounding platform and be complementary to the effusive activity.

[53] We also observe that seismicity accompanies both intrusions, but the exact temporal relationship to the intrusions is unclear. While for E2, surface deformation is not yet recorded after 6 h from the first earthquake, for E3 a partial amount of the total displacement is already recorded after 8 h from the first major shock. We also observe that, at least for E3, seismicity continues during the intrusion and stops once it is completed. If these earthquakes have tectonic origin they could represent the trigger mechanism for the subvolcanic intrusions. The same seismicity could also be a consequence of the intrusion itself and represent the brittle response of the crust to a volcanic intrusion, or be the combination of both mechanisms.

6.3.1. Caldera Subsidence and Collapse

[54] An important aspect of the inferred intrusions is their effect on the summit caldera. We have shown that rapid subsidence of the caldera floor occurred during both events (-0.10 m during E2 and -0.31 m during E3). If this subsidence is considered as volumes of magma withdrawn from the storage system, we demonstrate that comparable volumes of magma are erupted at the surface or intruded a depth.

[55] For the two intrusions studied here the measured deformation represents the elastic response of the overlying portion of the edifice to the pressure decrease within the reservoir but, if larger volumes of magma are withdrawn, the pressure within the system could drop enough to satisfy the failure criteria and cause the onset of a piston-like collapse. Furthermore, the transfer of magma to the flanks during the intrusions expands the volcanic

edifice and widens the fractures bounding the block overlying the reservoir, facilitating its downward sliding. If freed to descend, the piston can accelerate the process by pushing more magma toward the deeper reservoir. This mechanism could explain the 1968 caldera collapse and the discrepancy between the volume of magma erupted at the surface prior to the collapse and the volume of the collapse itself. The estimated $1\text{--}2 \text{ km}^3$ of magma (total volume of the collapse) could have withdrawn from the shallow reservoir from a combination of both eruptive (0.02 km^3) and intrusive activity. Multiple intrusions could have occurred and continued during the 12 days of the collapse. Evidence could be found in the incremental collapse inferred from the seismicity that accompanied this event [Stix and Kobayashi, 2008]. A feedback mechanism with the flank intrusions widening the edifice and enabling the downward motion of the piston, and the piston increasing the pressure within the system and pushing more magma toward the intrusions could have generated a large portion of the total volume of the collapse.

7. Conclusions

[56] We use single interferograms, LOS displacement time series and the modeling of the observed deformation to study the volcanic activity at Fernandina Volcano. We interpret the surface displacement as the expression of magmatic sources embedded within the volcanic edifice.

[57] 1. The shallow magma storage system is composed of two reservoirs at different depths, modeled as a shallower flat-topped body at $\sim 1.1 \text{ km}$ b.s.l. and a deeper ellipsoidal cavity at $\sim 4.9 \text{ km}$ b.s.l. Our findings are in agreement with previous geodetic and petrologic studies. Similar and recurrent patterns of deformation during the eight-year-long study period are interpreted as the activity of long-term magma reservoirs.

[58] 2. The two magma reservoirs are hydraulically connected given the rapid and contemporary response to pressure release events such as eruptions and subvolcanic lateral intrusions.

[59] 3. Further insights into the magma migration and reservoir dynamics are provided by post-eruptive/post-intrusive phases. Re-filling of the shallower reservoir first characterizes post-eruptive phases, while contemporary re-filling of both reservoirs occurs after deep lateral intrusions. We propose that pressure gradients within the plumbing system, together with different stiffness/compliance of the inferred sources, control the source activity when pressure increases.

[60] 4. In two occasions (December 2006 and August 2007), sills departing from the deeper reservoir intruded under the southern flank of the volcano generating broad uplift. A similar mechanism could explain the rapid deformation observed at Punta Espinoza in 1927. Earthquake swarms are associated with both intrusions. This seismicity could have tectonic origin and act as a trigger mechanism for the intrusion. It also could simply be the consequence of magma movement through the brittle crust or a combination of both.

[61] 5. Magma withdrawal from the shallow storage system and pressure decrease during intrusions also cause the rapid subsidence of the summit and the caldera floor. This aspect is important to understand the dynamics of the

summit caldera and can be used to explain the discrepancy between the volume of the 1968 collapse and the volume of the magma erupted prior to the event. During this event magma likely migrated downward from the shallow reservoir and largely intruded at depth causing the removal of the necessary support to the overlying block and triggered an incremental caldera collapse.

[62] **Acknowledgments.** This research was supported by the National Science Foundation (EAR 0838493) and NASA (graduate assistantship for Marco Bagnardi). ENVISAT radar data were provided by the European Space Agency through a Cat-1 project. The manuscript was greatly improved by helpful reviews from D. Geist and an anonymous reviewer. The authors would also like to thank M. Poland and M. Battaglia for constructive discussions.

References

- Allan, J., and T. Simkin (2000), Fernandina volcano's evolved, well-mixed basalts: Mineralogical and petrological constraints on the nature of the Galápagos plume, *J. Geophys. Res.*, **105**, 6017–6041, doi:10.1029/1999JB900417.
- Amelung, F., S. Jónsson, H. Zebker, and P. Segall (2000), Widespread uplift and “trapdoor” faulting on Galápagos volcanoes observed with radar interferometry, *Nature*, **407**, 993–996, doi:10.1038/35039604.
- Baker, M. S. (2012), Investigating the dynamics of basaltic volcano magmatic systems with space geodesy, PhD dissertation, Univ. of Miami, Miami, Fla.
- Berardino, P., G. Fornari, R. Lanari, and E. Sansosti (2002), A new algorithm for surface deformation monitoring based on small baseline differential SAR interferograms, *IEEE Trans. Geosci. Remote Sens.*, **40**(11), 2375–2383, doi:10.1109/TGRS.2002.803792.
- Bourquin, J., S. Hidalgo, B. Bernard, P. Ramón, S. Vallejo, and A. Parmigiani (2009), April 2009 Fernandina volcano eruption, Galápagos Islands, Ecuador: SO₂ and thermal field—Measurements compared with satellite data, informal report, Inst. Geofis. Escuela Politéc. Nac., Quito.
- Brooks, B. A., and L. N. Frazer (2005), Importance reweighting reduces dependence on temperature in Gibbs samplers: An application to the coseismic geodetic inverse problem, *Geophys. J. Int.*, **161**, 12–20, doi:10.1111/j.1365-246X.2005.02573.x.
- Casu, F., A. Manconi, A. Pepe, and R. Lanari (2011), Deformation time-series generation in areas characterized by large displacement dynamics: The SAR amplitude Pixel-Offset SBAS technique, *IEEE Trans. Geosci. Remote Sens.*, **49**(7), 2752–2763, doi:10.1109/TGRS.2010.2104325.
- Chadwick, W., and K. A. Howard (1991), The pattern of circumferential and radial eruptive fissures on the volcanoes of Fernandina and Isabela Islands, Galápagos, *Bull. Volcanol.*, **53**, 259–275, doi:10.1007/BF00414523.
- Chadwick, W., S. Jónsson, D. Geist, M. Poland, D. Johnson, S. Batt, K. Harpp, and A. Ruiz (2011), The May 2005 eruption of Fernandina volcano, Galápagos: The first circumferential dike intrusion observed by GPS and InSAR, *Bull. Volcanol.*, **73**(6), 679–697, doi:10.1007/s00445-010-0433-0.
- Chen, C. W., and H. Zebker (2001), Two-dimensional phase unwrapping with use of statistical models for cost functions in nonlinear optimization, *J. Opt. Soc. Am. A Opt. Image Sci. Vis.*, **18**, 338–351, doi:10.1364/JOSAA.18.000338.
- Couffer, J. (1956), The disappearance of Urvina Bay, *Nat. Hist.*, **65**, 378–383.
- Cullen, A. B., A. R. McBirney, and R. D. Rogers (1987), Structural controls on the morphology of Galápagos shields, *J. Volcanol. Geotherm. Res.*, **34**, 143–151, doi:10.1016/0377-0273(87)90099-0.
- Del Negro, C., G. Currenti, and D. Scandura (2009), Temperature-dependent viscoelastic modeling of ground deformation: Application to Etna volcano during the 1993–1997 inflation period, *Phys. Earth Planet. Inter.*, **172**, 299–309, doi:10.1016/j.pepi.2008.10.019.
- De Natale, G., and F. Pingue (1996), Ground deformation modelling in volcanic areas, in *Monitoring and Mitigation of Volcano Hazards*, edited by R. Scarpa and R. Tilling, pp. 365–388, Springer, New York, doi:10.1007/978-3-642-80087-0_11.
- Feighner, M., and M. Richards (1994), Lithospheric structure and compensation mechanisms of the Galapagos Archipelago, *J. Geophys. Res.*, **99**, 6711–6729.
- Fialko, Y., Y. Khazan, and M. Simons (2001), Deformation due to a pressurized horizontal circular crack in an elastic half-space, with applications to volcano geodesy, *Geophys. J. Int.*, **146**, 181–190, doi:10.1046/j.1365-246X.2001.00452.x.
- Filson, J., T. Simkin, and L. K. Leu (1973), Seismicity of a caldera collapse, Galápagos Islands 1968, *J. Geophys. Res.*, **78**, 8591–8622, doi:10.1029/JB078i035p08591.
- Foroozan, R., D. Elsworth, B. Voight, and G. S. Mattioli (2010), Dual reservoir structure at Soufrière Hills Volcano inferred from continuous GPS observations and heterogeneous elastic modeling, *Geophys. Res. Lett.*, **37**, L00E12, doi:10.1029/2010GL042511.
- Geist, D. (2011), An evolutionary model of Galapagos magma chambers, paper presented at 2011 Chapman Conference—The Galápagos as a Laboratory for the Earth Science, AGU, Puerto Ayora, Ecuador.
- Geist, D., T. Naumann, and P. Larson (1998), Evolution of Galapagos magmas: Mantle and crystal fractionation without assimilation, *J. Petrol.*, **39**(5), 953–971, doi:10.1093/petroj/39.5.953.
- Geist, D., W. Chadwick, and D. Johnson (2006a), Results from new GPS and gravity monitoring networks at Fernandina and Sierra Negra volcanoes, Galápagos, 2000–2002, *J. Volcanol. Geotherm. Res.*, **150**, 79–97, doi:10.1016/j.volgeores.2005.07.003.
- Geist, D., D. J. Fornari, M. D. Kurz, K. S. Harpp, S. A. Soule, M. R. Perfitt, and A. M. Koleszar (2006b), Submarine Fernandina: Magmatism at the leading edge of the Galápagos hot spot, *Geochem. Geophys. Geosyst.*, **7**, Q12007, doi:10.1029/2006GC001290.
- Gourmelen, N., F. Amelung, and R. Lanari (2010), Interferometric synthetic aperture radar–GPS integration: Interseismic strain accumulation across the Hunter Mountain fault in the eastern California shear zone, *J. Geophys. Res.*, **115**, B09408, doi:10.1029/2009JB007064.
- Hey, R. N. (1977), Tectonic evolution of the Cocos-Nazca spreading center, *Geol. Soc. Am. Bull.*, **88**, 1414–1420.
- Howard, K. A. (2010), Caldera collapse: Perspectives from comparing Galápagos volcanoes, nuclear-test sinks, sandbox models, and volcanoes on Mars, *GSA Today*, **20**(10), 4–10, doi:10.1130/GSATG82A.1.
- Jónsson, S. (2009), Stress interaction between magma accumulation and trapdoor faulting on Sierra Negra volcano, Galápagos, *Tectonophysics*, **471**(1–2), 36–44, ISSN doi:10.1016/j.tecto.2008.08.005.
- Jónsson, S., H. Zebker, P. Cervelli, P. Segall, H. Garbeil, P. Mouginis-Mark, and S. Rowland (1999), A shallow-dipping dike fed the 1995 flank eruption at Fernandina Volcano, Galápagos, observed by satellite radar interferometry, *Geophys. Res. Lett.*, **26**(8), 1077–1080, doi:10.1029/1999GL900108.
- Jónsson, S., H. Zebker, P. Segall, and F. Amelung (2002), Fault slip distribution of the 1999 Mw7.1 Hector Mine earthquake, California, estimated from satellite radar and GPS measurements, *Bull. Seismol. Soc. Am.*, **92**, 1377–1389, doi:10.1785/020000922.
- Lanari, R., O. Mora, M. Manunta, J. J. Mallorqui, P. Berardino, and E. Sansosti (2004), A small-baseline approach for investigating deformations on full-resolution differential SAR interferograms, *IEEE Trans. Geosci. Remote Sens.*, **42**, 1377–1386, doi:10.1109/TGRS.2004.828196.
- Manconi, A., T. R. Walter, and F. Amelung (2007), Effects of mechanical layering on volcano deformation, *Geophys. J. Int.*, **170**, 952–958, doi:10.1111/j.1365-246X.2007.03449.x.
- Massonnet, D., K. Feigl, M. Rossi, and F. Adragna (1994), Radar interferometric mapping of deformation in the year after the Landers earthquake, *Nature*, **369**, 227–230, doi:10.1038/369227a0.
- Masterlark, T., M. Haney, H. Dickinson, T. Fournier, and C. Searcy (2010), Rheology and structural controls on the deformation of Okmok volcano, Alaska: FEMS, InSAR and ambient noise tomography, *J. Geophys. Res.*, **115**, B02409, doi:10.1029/2009JB006324.
- McTigue, D. F. (1987), Elastic stress and deformation near a finite spherical magma body: Resolution of the point source paradox, *J. Geophys. Res.*, **92**, 12,931–12,940.
- Mogi, K. (1958), Relations between the eruptions of various volcanoes and the deformations of the ground surfaces around them, *Bull. Earthquake Res. Inst. Univ. Tokyo*, **36**, 99–134.
- Montgomery-Brown, E. K., P. Segall, and A. Miklius (2009), Kilauea slow slip events: Identification, source inversions, and relation to seismicity, *J. Geophys. Res.*, **114**, B00A03, doi:10.1029/2008JB006074.
- Morgan, W. J. (1971), Convection plumes in the lower mantle, *Nature*, **230**, 42–43, doi:10.1038/230042a0.
- Okada, Y. (1992), Internal deformation due to shear and tensile faults in a half-space, *Bull. Seismol. Soc. Am.*, **82**, 1018–1040.
- Pepe, A., and R. Lanari (2006), On the extension of the minimum cost flow algorithm for phase unwrapping of multitemporal differential SAR interferograms, *IEEE Trans. Geosci. Remote Sens.*, **44**, 2374–2383, doi:10.1109/TGRS.2006.873207.
- Richards, A. (1957), Volcanism in eastern Pacific Ocean basin: 1945–1955, *Proc. Int. Geol. Congr.*, **20**, 19–31.
- Rivalta, E. (2010), Evidence that coupling to magma chambers controls the volume history and velocity of laterally propagating intrusions, *J. Geophys. Res.*, **115**, B07203, doi:10.1029/2009JB006922.

- Rivalta, E., and P. Segall (2008), Magma compressibility and the missing source for some dike intrusions, *Geophys. Res. Lett.*, **35**, L04306, doi:10.1029/2007GL032521.
- Rosen, P. A., S. Henley, G. Peltzer, and M. Simons (2004), repeat orbit interferometry package released, *Eos Trans. AGU*, **85**(5), 47, doi:10.1029/2004EO050004.
- Rowland, S. K., and D. Munro (1992), The caldera of Volcan Fernandina: A remote sensing study of its structure and recent activity, *Bull. Volcanol.*, **55**, 97–109, doi:10.1007/BF00301123.
- Rowland, S. K., A. J. L. Harris, M. J. Wooster, F. Amelung, H. Garbeil, L. Wilson, and P. J. Mouginis-Mark (2003), Volumetric characteristics of lava flows from interferometric radar and multispectral satellite data: The 1995 Fernandina and 1998 Cerro Azul eruptions in the western Galapagos, *Bull. Volcanol.*, **65**, 311–330, doi:10.1007/s00445-002-0262-x.
- Segall, P. (2010), *Earthquake and Volcano Deformation*, 432 pp., Princeton Univ. Press, Princeton, N. J.
- Simkin, T. (1984), Geology of Galápagos Islands, in *Galápagos*, edited by R. Perry, pp. 15–41, Pergamon, Oxford, U. K.
- Simkin, T., and K. A. Howard (1970), Caldera collapse in the Galápagos Islands, 1968, *Science*, **169**, 429–437, doi:10.1126/science.169.3944.429.
- Stix, J., and T. Kobayashi (2008), Magma dynamics and collapse mechanisms during four historic caldera-forming events, *J. Geophys. Res.*, **113**, B09205, doi:10.1029/2007JB005073.
- Tiamo, K. F., J. B. Rundle, J. Fernández, and J. Langbein (2000), Spherical and ellipsoidal volcanic sources at Long Valley Caldera, California using a Genetic Algorithm inversion technique, *J. Volcanol. Geotherm. Res.*, **102**, 189–206.
- Villagómez, D. R., D. R. Toomey, E. E. E. Hooft, and S. C. Solomon (2007), Upper mantle structure beneath the Galápagos Archipelago from surface wave tomography, *J. Geophys. Res.*, **112**, B07303, doi:10.1029/2006JB004672.
- Williams, C. A., and G. Wadge (1998), The effects of topography on magma chamber deformation models: Application to Mt. Etna and radar interferometry, *Geophys. Res. Lett.*, **25**, 1549–1552, doi:10.1029/98GL01136.
- Wilson, J. T. (1963), A possible origin of the Hawaiian islands, *Can. J. Phys.*, **41**, 863–870, doi:10.1139/p63-094.
- Yang, X. M., P. Davis, and J. H. Dietrich (1988), Deformation from inflation of a dipping finite oblate spheroid in an elastic half-space as a model for volcanic stressing, *J. Geophys. Res.*, **93**, 4249–4257, doi:10.1029/JB093iB05p04249.
- Yun, S., P. Segall, and H. Zebker (2006), Constraints on magma chamber geometry at Sierra Negra Volcano, Galápagos Islands, based on InSAR observations, *J. Volcanol. Geotherm. Res.*, **150**, 232–243, doi:10.1016/j.jvolgeores.2005.07.009.